Supplementary Information for:

Deciphering 2D Perovskite's Role in Perovskite Solar Cells via Intact 3D/2D Junctions

Seungmin Lee[a,b], Hyeonah Cho [a], Sohyun Kang[a], Oui Jin Oh[a], Dong Hyun Kim [a], and Jun Hong Noh [a,c,*]

[a] School of Civil, Environmental and Architectural Engineering, Korea University, Seoul 02841,

Republic of Korea

[b] Department of Integrative Energy Engineering and KU-KIST Green School Graduate School of Energy and Environment, Korea University, Seoul 2841, Republic of Korea

*Corresponding author: junhnoh@korea.ac.kr (J. H. N.)

[†] These authors contributed equally

Material and method

Materials

Urea, hydrochloric acid (HCl, 37%), thioglycolic acid (TGA), potassium chloride (KCl, 99.999%), dimethyl sulfoxide (DMSO, ≥99.9%), N,N-Dimethylformamide (DMF, 99.8%), Acetonitrile (ACN, 99.8%), 1-Methyl-2-pyrrolidinone (NMP, 99.95%), Chlorobenzene (CB, 99.8%), Bis(trifluoromethane)sulfonimide lithium salt (Li-TFSI, 99.95%) and 4-tert-Butylpyridine (t-BP, 98%) were purchased from Sigma Aldrich. Formamidinium iodide (FAI, >99.99%), Methylammonium chloride (MACl, >99.99%), n-Butylammonium bromide (BABr, >99%) were purchased from Greatcell solar. Lead (II) iodide (PbI_2, 99.99%), Lead(II) bromide ($PbBr_2$, >98%) were purchased from the Tokyo Chemical Industry. 2,2′,7,7′-tetrakis[N,N-di(4-methoxyphenyl)amino]-9,9′-spirobifluorene (spiro-OMeTAD) and tris(2-(1H-pyrazol-1-yl)-4-tert-butylpyridine)cobalt(III) tri[bis(trifluoromethane)sulfonamide (FK209) were purchased from Lumtec. Tin(II) chloride dihydrate was purchased from Alfa Aesar. Diethyl ether (99.5%) was purchased from SAMCHUN.

Device fabrication

$FAPbI_3$ micro powder synthesis

The black alpha-form of $FAPbI_3$ micro powder was synthesized using a 0.8 M precursor solution of FAI and PbI_2 in 33 ml of 2-Me. The solution, stirred with a stirring bar, was heated to 120°C in an oil bath and then subjected to precipitation using the retrograde method for 3 hours. The precipitated $FAPbI_3$ micro powder was filtered and subsequently baked at 150°C for 30 minutes.

Preparing the precursor solution for 2D perovskite

Precursor solutions for the compositions $(BA)_2PbI_4$ and $(BA)_2PbBr_4$ are prepared at concentrations of 0.2 M and 0.1 M, respectively. Specifically, for $(BA)_2PbI_4$, BAI and PbI_2 are dissolved in a 2:1 molar ratio in a mixed solvent, consisting of DMF and DMSO combined at a 9:1 (volume ratio). The BA_2PbBr_4 precursor solution is prepared similarly, using the same mixed solvent.

Preparing the precursor solution for 3D perovskite

A 1.8 M perovskite precursor solution with the composition of $FAPbI_3$ was prepared by dissolving 1.317 g (2.08 mmol) of $FAPbI_3$ and 0.0492 g (0.728 mmol) of MACl in 1.01 ml (0.951g) of DMF, combined with 0.15 ml (0.1625g, 2.08 mmol) of DMSO.

Electron transport layer fabrication

Prepatterned Asahi FTO substrates were sequentially cleaned with deionized water, acetone, ethanol, and 2-propanol, each for 15 minutes. The substrates were then exposed to UV/O_3 for 30 minutes to prepare the surface for tin oxide (SnO_2) deposition. For the SnO_2 layer, 2.2 g of $SnCl_2 \cdot 2H_2O$ and 10 g of urea were dissolved in a mixture of 200 µl of thioglycolic acid, 10 ml of HCl, and 800 ml of deionized water. The FTO substrates were immersed in this solution at 90°C for 6 hours. Afterwards, the substrates were heat-treated at 150°C for 6 hours. The thickness of the SnO_2 layer was confirmed to be 40 nm.

2D perovskite film fabrication

Tin-doped indium oxide (ITO)-coated glass substrates were sequentially cleaned using deionized water, acetone, ethanol, and isopropyl alcohol, each for 15 minutes. To enhance the wetting of the 2D perovskite precursor solution, substrates were exposed to ultraviolet-ozone treatment for 15 minutes. The 2D perovskite precursor solution was then spin-coated onto the substrates at 5,000 rpm for 20 seconds, during which 1 mL of diethyl ether was rapidly applied at the 10 seconds. Immediately after coating, the films were transferred to a hot plate and heat-treated at 100°C for 5 minutes. It is advised to produce the 2D perovskite films under 30-40% relative humidity for optimal results.

3D perovskite film fabrication

The FTO/SnO_2 substrates were further treated with UV/O_3 for an additional 15 minutes. A 30 mM KCl solution in deionized water was then spin-coated onto the substrates at 5000 rpm (acc. 2500 rpm/s) for 30 seconds. Subsequently, the substrates were annealed at 150°C for 10 minutes. Following this, 70 µL of the previously described 3D perovskite precursor solution was applied to the FTO/SnO_2 substrates using a two-step spin-coating process: initially at 1000 rpm for 3 seconds, followed by 5000 rpm for 10 seconds. Just one second before the conclusion of the second step, 1 mL of diethyl ether was swiftly applied to the spinning substrate. The resulting yellow film was immediately transferred to a hot plate and annealed at 120°C for 100 minutes. For 3D perovskite, it is typically formed with a thickness of 730 nm.

3D/SIG-2D bilayer fabrication via solid-state in-plane growth

A hot-press method was employed to fabricate the 3D/SIG-2D film. Initially, the surfaces of the pre-prepared solid 2D and 3D films were aligned to ensure contact. Subsequently, these contacted films were pressed at 60 MPa for 10 minutes at specified temperatures of 30°C, 45°C, or 60°C. Unless otherwise specified, the 3D/SIG-2D bilayers in this study were fabricated under the conditions of 60°C, 10 minutes, and 60 MPa.

Hole transport layer and counter electrode fabrication

The Spiro-OMeTAD solution was prepared by adding 23 µL of Li-TFSI solution (540 mg/mL in acetonitrile), 10 µL of FK209 solution (376 mg/mL in acetonitrile), and 39 µL of t-butylpyridine to 100 mg of spiro-OMeTAD dissolved in 1.1 mL of chlorobenzene. The solution was then dynamically spin-coated onto both 3D and 3D/SIG-2D films at 2,000 rpm for 30 seconds. The thickness of Spiro-OMeTAD was confirmed to be ~ 200nm. Subsequently, a gold electrode was deposited by thermal evaporation to a thickness of approximately 130 nm, with the deposition area of the counter electrode fixed at 0.16 cm².

For space-charge-limited current (SCLC) measurements, Me-2PACz was dissolved in isopropyl alcohol (IPA) at a concentration of 0.1 mg/ml. Approximately 0.1 ml of this solution was dispensed onto an FTO glass substrate and allowed to rest for 10 seconds before being spin-coated at 6000 rpm (acc. 6000 rpm/s) for 30 seconds. Subsequently, the coated substrate underwent heat treatment at 100°C for 5 minutes. This coating and heating process was repeated twice to enhance reproducibility.

Characterization
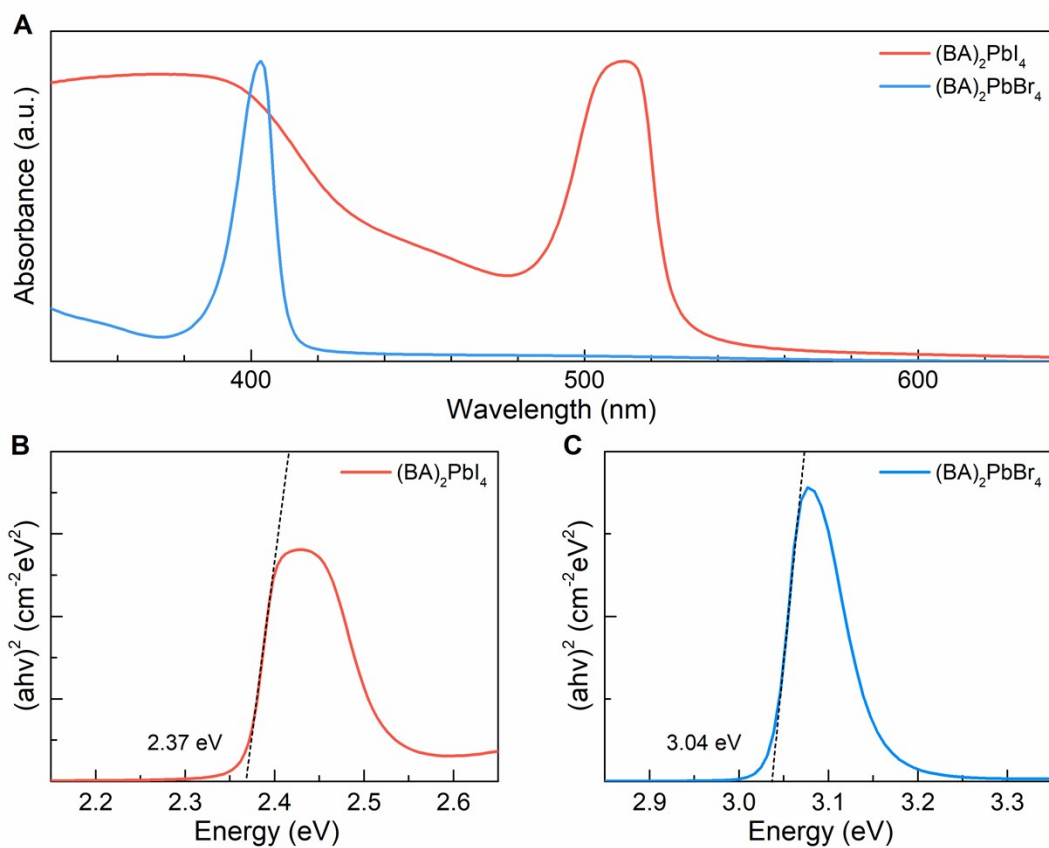
Film characterization

Optical properties of the films were measured through UV-vis spectroscopy (Cary 5000, Agilent Technologies). UPS spectra were obtained using an Axis-Supra (Kratos) with He I (21.2 eV) UV source. XRD spectra were measured by using a Rigaku SmartLab with a 9 kW Cu target X-ray generator. TOF-SIMS measurement was conducted by using a time-of-flight secondary-ion mass spectrometer (ION-TOF) equipped with a 1 keV Cs^+ ion beam for the sputtering and 30 keV Bi^+ pulsed primary ion beam for the analysis. XPS analysis was measured by using Axis Supra⁺ (Kratos) equipment with Al Kα as the X-ray source. SEM measurements were carried out using a Field Emission Scanning Electron Microscopy (FEI Quanta FEG 250). The steady-state PL was measured using a 485 nm diode laser (Horiba, DeltaDiode-485L). Photon escaping from the perovskite films were collected using the double-grating monochromator (Horiba, FL-1005) and a liquid-nitrogen-cooled low noise photomultiplier tube (Hamatsu, R5509-43). TRPL was implemented using the pulsed mode of the diode laser with 485 nm (Horiba, DeltaDiode-485L-CW). PLQE measurement was performed with 3.2inch diameter integrated sphere (Horiba, FL-sphere). The PLQE was calculated using the photoluminescence (PL) spectrum under three different conditions: i) reference laser intensity, ii) indirect excitation, and iii) direct excitation[1]. All UPS measurements were conducted following standard procedures, with a -9V bias applied between the samples and the detectors to enhance the signal[2]. KPFM data were obtained by using AFM NX-10 (Park Systems) in glove box. The real work function values of each perovskite sample were calculated by comparing the measured surface potential to the known 4.93 eV work function of the tip (HQ:NSC35/Pt).
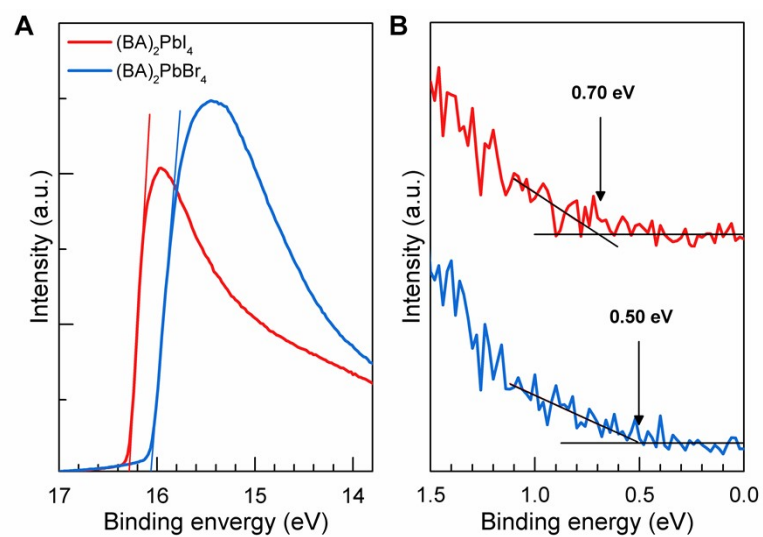
Device characterization

J-V characteristics were measured using a source meter (Keithley 2400) under the illumination of the solar simulator (Newport, Oriel Class AAA, 94043A) at AM 1.5G as checked with a Si-reference cell (KG with quartz and KG3) certificated by the National Renewable Energy Laboratory (NREL). The J-V curves were all measured with a scan speed of 100 mVs^{-1} and the step voltage of 10 mV. A reverse scan, starting at 1.2V and moving to -0.2V, was followed immediately by a forward scan, enabling the acquisition of two types of J-V curves. The active area was determined by the metal masks with circle-type (0.096 cm^2) placed in front of the PSCs. To obtain J-V curves as a function of light intensity, we adjusted the light intensity using four different neutral density (ND) filters, calibrated with a silicon reference cell. Subsequently, we recorded the J-V characteristics under these varied lighting conditions. The EQE measurements were conducted using a QUANTX-300 QE measurement, which utilized a 100 W xenon lamp as the light source and 130 mm focal length monochromator with dual gratings. ELQEs were measured using a calibrated silicon photodiode (Hamamatsu, S1227-1010BQ), which possesses a larger collection area than the active area of the device. Both the injection current from the source meter (Keithley 2450) and the photocurrent detected by the photodiode were controlled and recorded using the 'SweepMe!' software[3]. Mott-Schottky plot was performed using the potentiostat (IviumStat.h, Ivium Technologies). All devices with full structure underwent a reverse scan from 1.2 V to -0.2 V at 10 kHz via scan rate of 2mV/s and interval of 10 mV. Prior to scanning, each device was preconditioned with a bias voltage of 1.2 V for 100 seconds to accurately delineate the depletion region for the Mott-Schottky plot[4].

Stability test

All stability measurements were conducted on devices encapsulated with a 1.1 mm cover glass, PIB tape [5], and UV-curing resin (Three Bond, 3052B)[6, 7]. Initially, the non-functional corners of the device were removed using 2-methoxyethanol. Subsequently, PIB tape was positioned between the device and the cover glass to facilitate primary encapsulation, during which pressure was applied. In the second stage, the edges of the device were sealed with UV-curing resin and subsequently hardened under a 365 nm UV lamp. MPPT testing was conducted using a custom-built system, comprising a source meter (Keithley 2450) and an LED solar simulator (Newport, LSH-7320).

Figure S1. **Optical properties of 2D perovskite films with the (BA)₂PbX₄ structure, where X represents iodide or bromide.** (A) UV-vis spectra and (B-C) Tauc plot for (BA)$_2$PbI$_4$ and (BA)$_2$PbBr$_4$ films on ITO.

Figure S2. Energy level characterization of 2D perovskite using ultraviolet photoelectron spectroscopy (UPS). (A) The work function (ϕ) of each film were determined using the onset of secondary electrons. (B) (Ionization energy – ϕ) value. The 2D perovskite results were obtained using thin films with an ITO/2D structure.
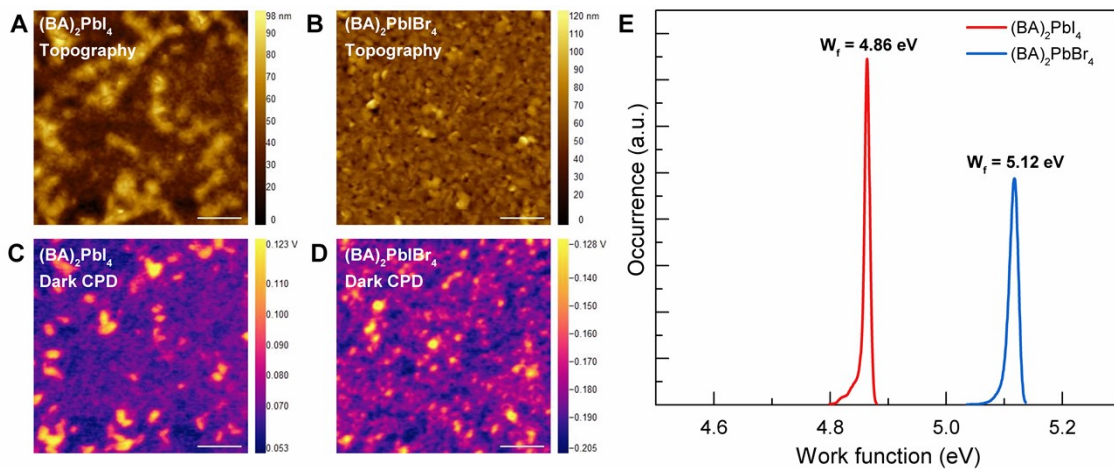
Figure S3. The work function characterization of 2D perovskite using the kelvin probe force microscope (KPFM). (A, B) Topography images of (BA)2PbI4 and (BA)2PbBr4 film on ITO substrate. (C, D) Contact potential difference (CPD) images in dark condition for corresponding films. (E) Distribution of ϕ derived from tip's work function. The ϕ of the tip is measured to be 4.93 eV.
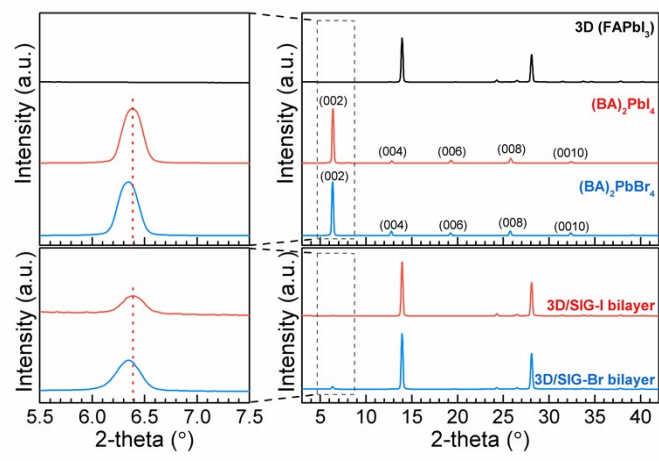
**Figure S4. X-ray Diffraction curves for 3D, (BA)₂PbI₄, (BA)2PbBr₄, 3D/SIG-I, and 3D/SIG-Br films.**

Table S1. 2D perovskite layer related peak position of (002), miller indices, and its full width at half maximum (FWHM) of (BA)$_2$PbI$_4$, (BA)$_2$PbBr$_4$, 3D/SIG-I, and 3D/SIG-Br films.

| Condition	Peak position (°)	Miller Indices	FWHM (°)
(BA)$_2$PbI$_4$	6.384	(002)	0.209
(BA)$_2$PbBr$_4$	6.344	(002)	0.212
3D/SIG-I	6.387	(002)$_{SIG-I}$	0.222
3D/SIG-Br	6.342	(002)$_{SIG-Br}$	0.276

Table S2. Light-harvesting layer related peak position, miller indices, lattice parameters, and FWHM

Condition	Peak position (°)	Miller Indices	Lattice parameter (Å)	FWHM (°)
3D (FAPbI$_3$)	13.938	(001)$_{3D}$	6.349	0.225
	28.089	(002)$_{3D}$	6.348	0.237
3D/SIG-I	13.939	(001)$_{3D}$	6.348	0.224
	28.089	(002)$_{3D}$	6.348	0.236
3D/SIG-Br	13.937	(001)$_{3D}$	6.349	0.222
	28.089	(002)$_{3D}$	6.348	0.237

of (BA)$_2$PbI$_4$, (BA)$_2$PbBr$_4$, 3D/SIG-I, and 3D/SIG-Br films.
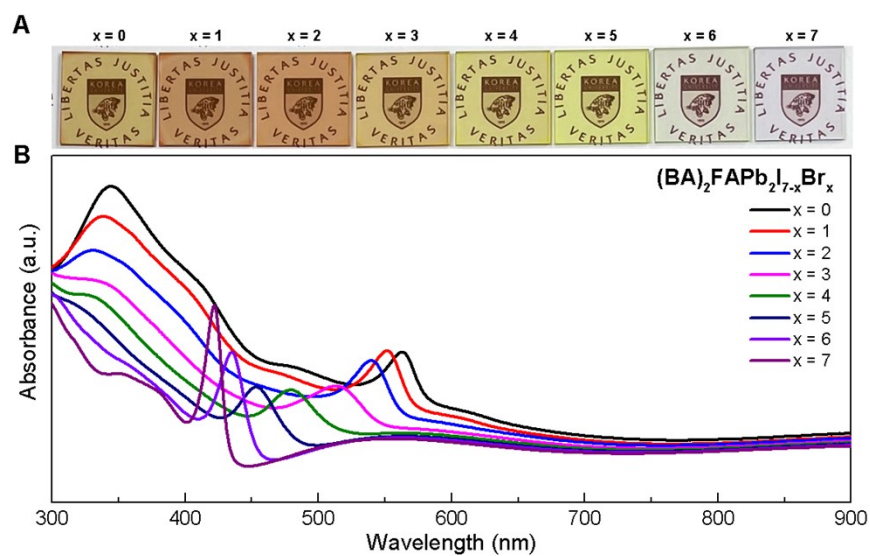
Figure S5. Characterization for n=2 phase qausi-2D films. (A) Photographic image for n=2 phase 2D perovskite films. (B) Absorbance spectrum for n=2 phase 2D perovskite films with composition of $(BA)_2FAPb_2I_{7-x}Br_x$. Each film was fabricated by the spin coating method by mixing BAI, BABr, FAI, FABr, PbI_2, and $PbBr_2$ to their respective compositions.
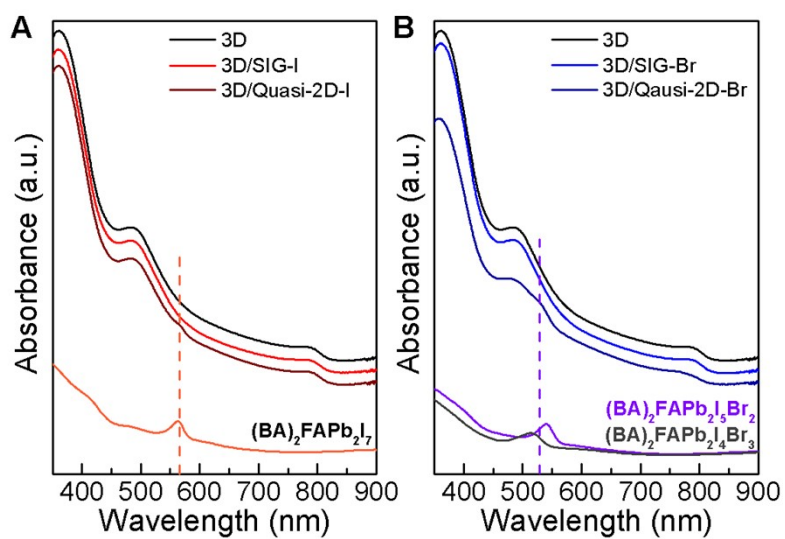
Figure S6. Characterization of absorbance spectrum for 3D, 3D/SIG-2D, and 3D/Quasi-2D using (A) (BA)$_2$PbI$_4$ and (B) (BA)$_2$PbBr$_4$ films. 3D/quasi-2D films were produced by heating each 2D film to 90 degrees while in contact with the surface of the 3D film.
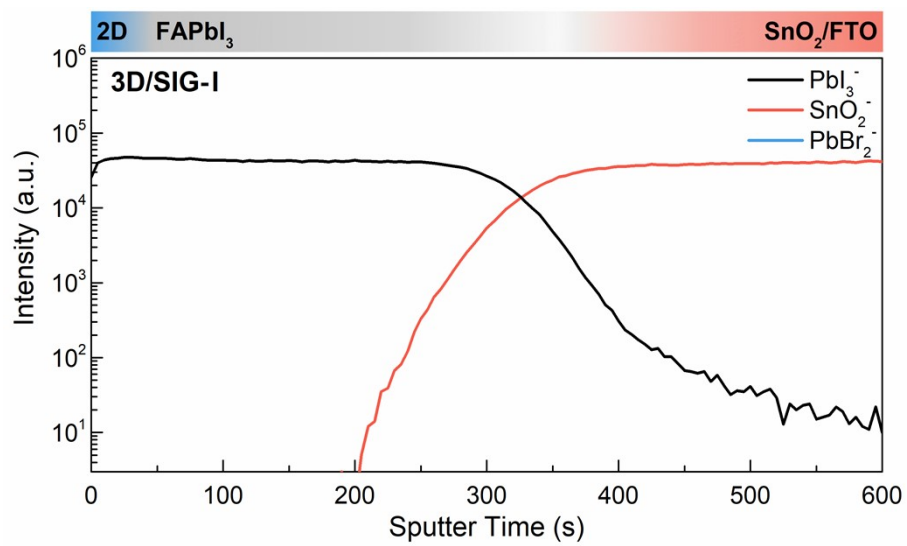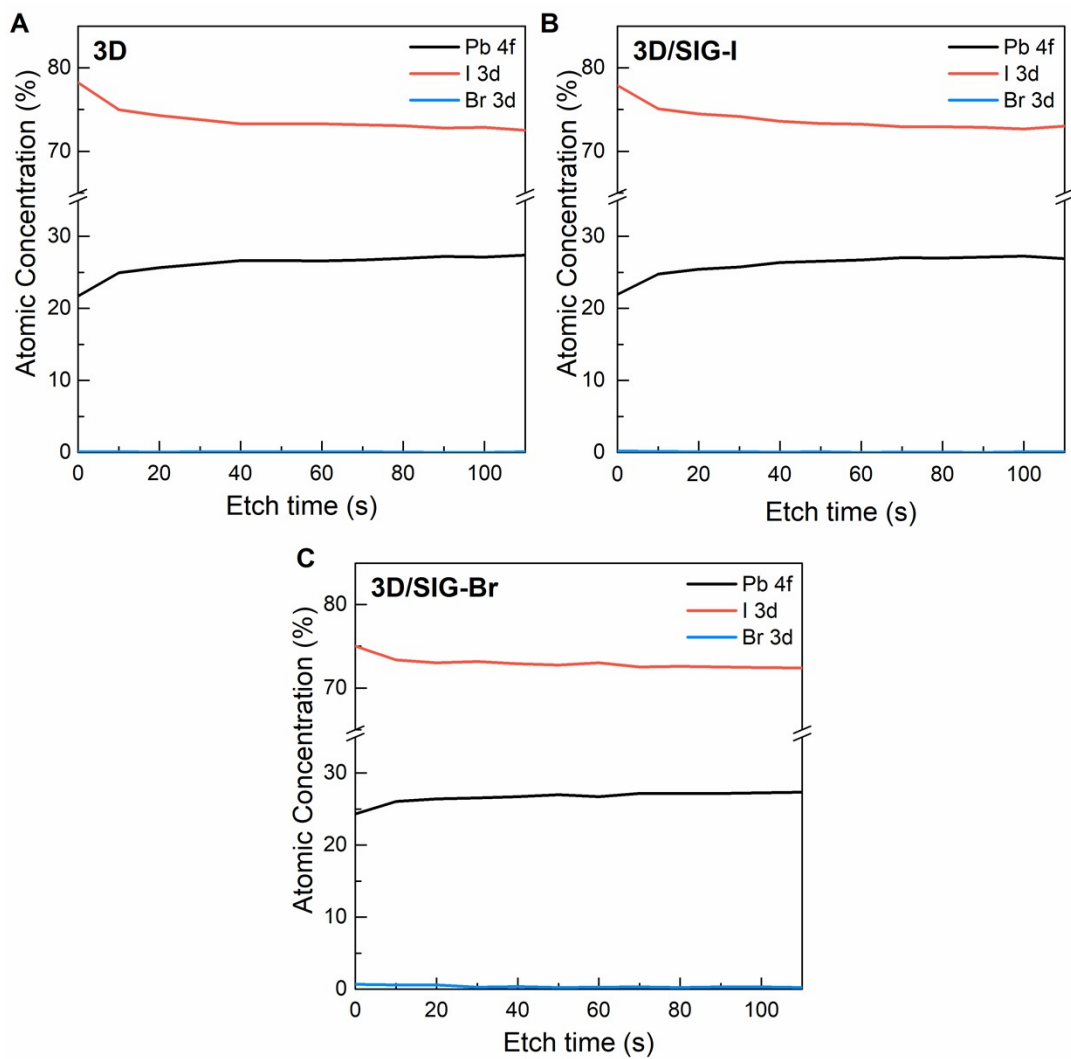
Figure S7. Elemental depth profile of 3D/SIG-I as obtained using Time-of-Flight Secondary Ion Mass Spectrometry.
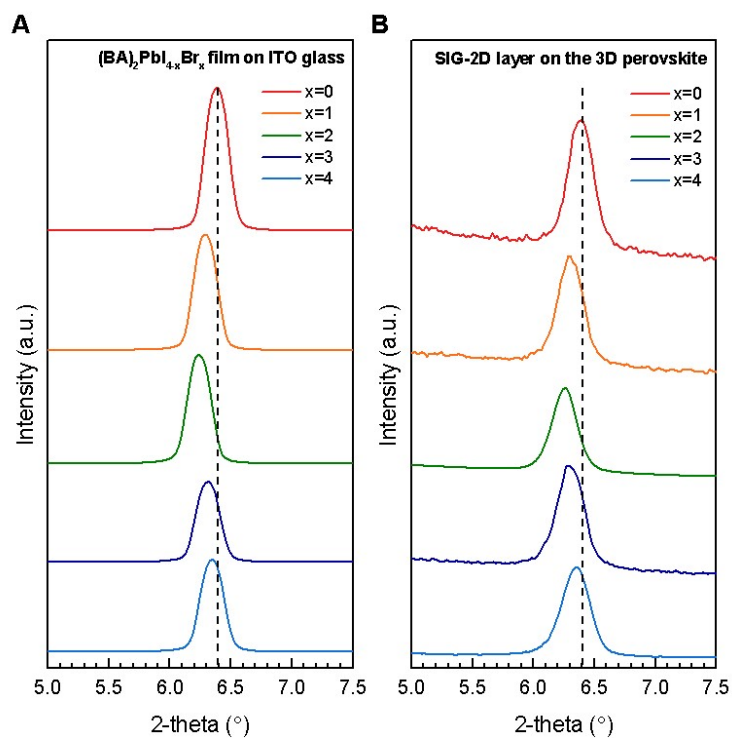
Figure S8. Comparison of X-ray Photoelectron Spectroscopy depth profiles. All samples, including (A) 3D, (B) 3D/SIG-I, and (C) 3D/SIG-Br films, were fabricated using the same process as that for photovoltaic device fabrication.

Table S3. Calculated ratios relative to Pb atoms for 3D, 3D/SIG-I, and 3D/SIG-Br films.

|	3D	3D/SIG-I	3D/SIG-Br
I/Pb	3.61	3.55	3.08
Br/Pb	0.00	0.00	0.03
(I+Br)/Pb	3.61	3.55	3.08

Figure S9. X-ray Diffraction curves for pure 2D perovskite and SIG-2D layer. (A) (002) peak of pure 2D perovskite according to composition of 2D perovskite with $(BA)_2PbI_{4-x}Br_x$, (B) (002) peak of SIG-2D layer on the 3D perovskite with various composition of 2D perovskite

**Table S4. Recombination lifetimes fitted from the PL decay for the control and SIG films.**

Condition	τ_1 (ns)	τ_2 (ns)
3D	44	588
3D/SIG-I	131	3937
3D/SIG-Br	135	3990
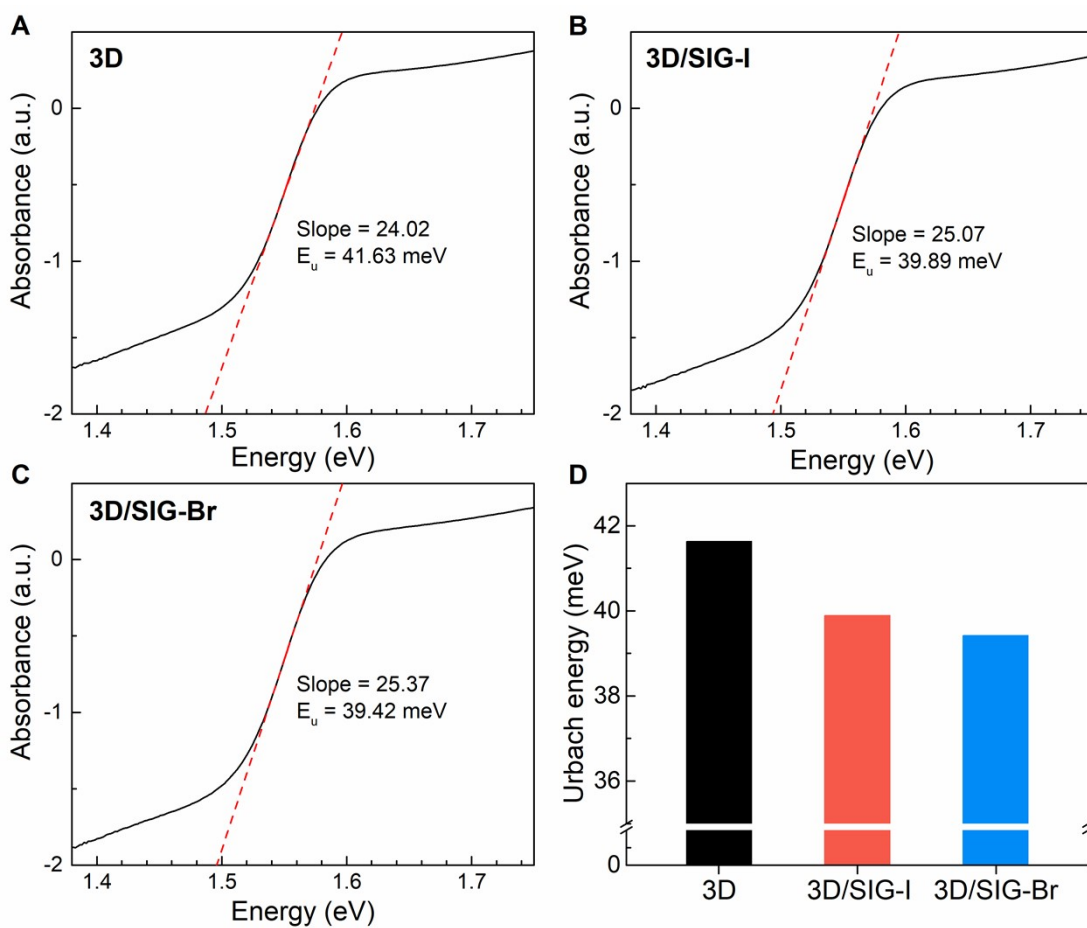
Figure S10. Urbach energy (E_u) calculated in perovskite films for all samples. E_u was calculated from the UV–vis absorption spectra according to the following equation. $\alpha = \alpha_0 exp(h\nu/E_u)$ where α is the absorption coefficient and $h\nu$ is the photon energy. [8-10]
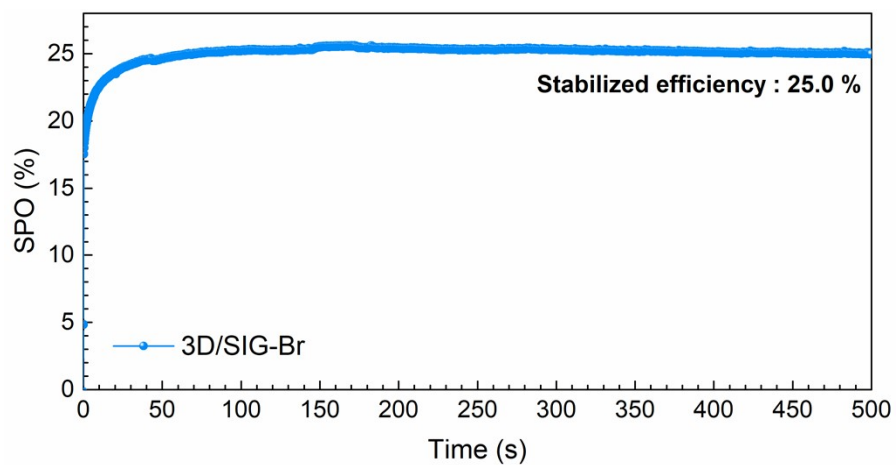
Figure S11. Stabilized power output (SPO) of 3D/SIG-Br device. SPO determined by holding the cell at a fixed voltage near the maximum power point (MPP) on the J–V curve for 500 s.
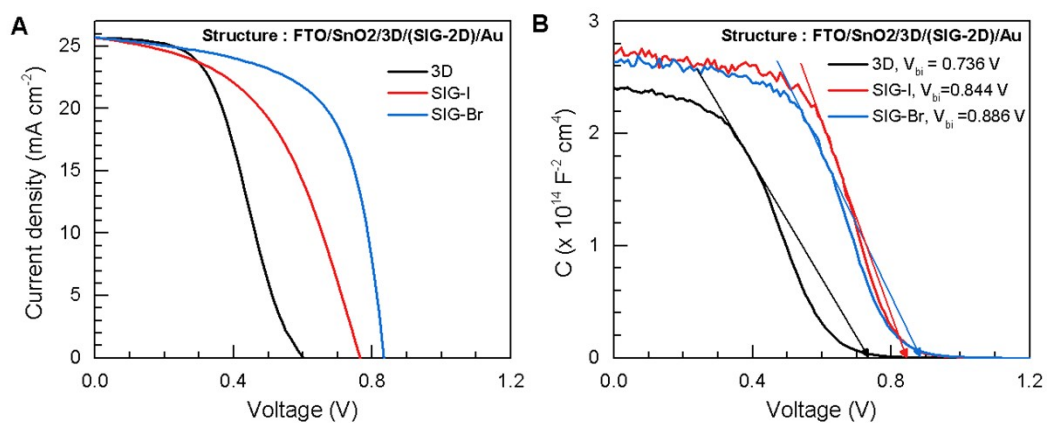
Figure S12. Characterization of HTL-free device. (A) Current density – voltage curve of 3D, SIG-I, and SIG-Br devices. (B) Mott-Schottky plot of 3D, SIG-I, and SIG-Br devices. All devices were fabricated with the same structure (FTO/SnO2/3D/(SIG-2D)/Au).
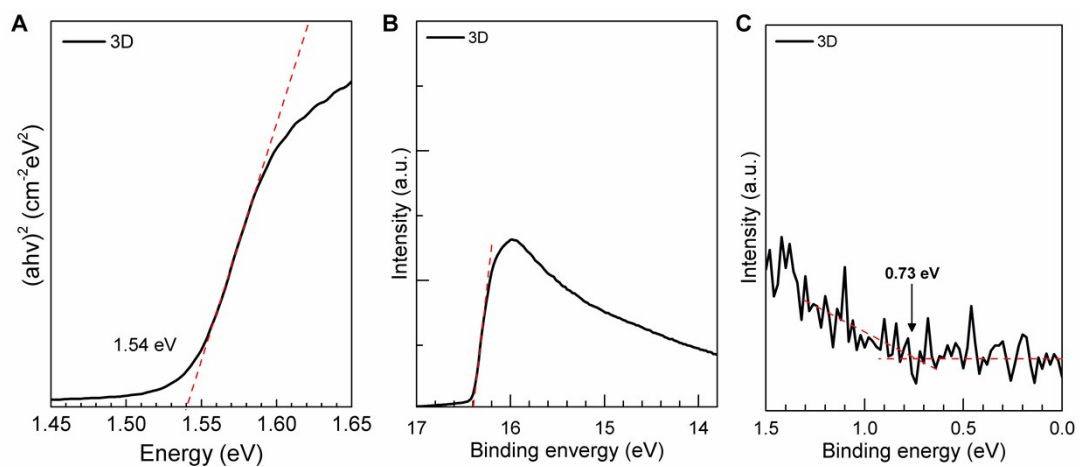
Figure S13. Energy level characterization of 3D perovskite using Tauc plot and UPS measurement.
(A) Tauc plot of 3D FAPbI$_3$ perovskite film for determining the optical band gap. (B) Results from UPS measurements to assess the (B) Φ and (C) (IE-Φ) value of 3D perovskite. The measured 3D perovskite was deposited on an FTO/SnO$_2$ substrate.
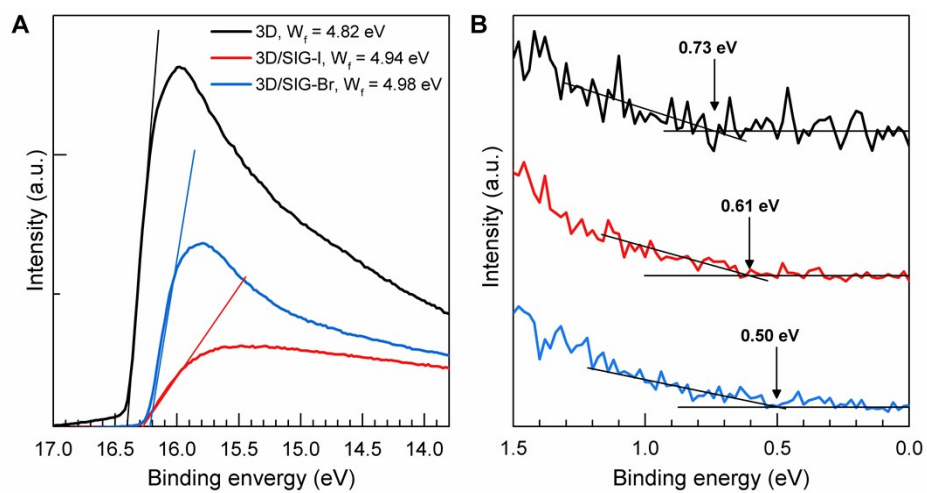
Figure S14. Energy level characterization of 3D/SIG-2D bilayer using UPS measurement. Results from UPS measurements to assess the (A) Φ and (B) (IE-Φ) value of 3D/SIG-2D bilayer.
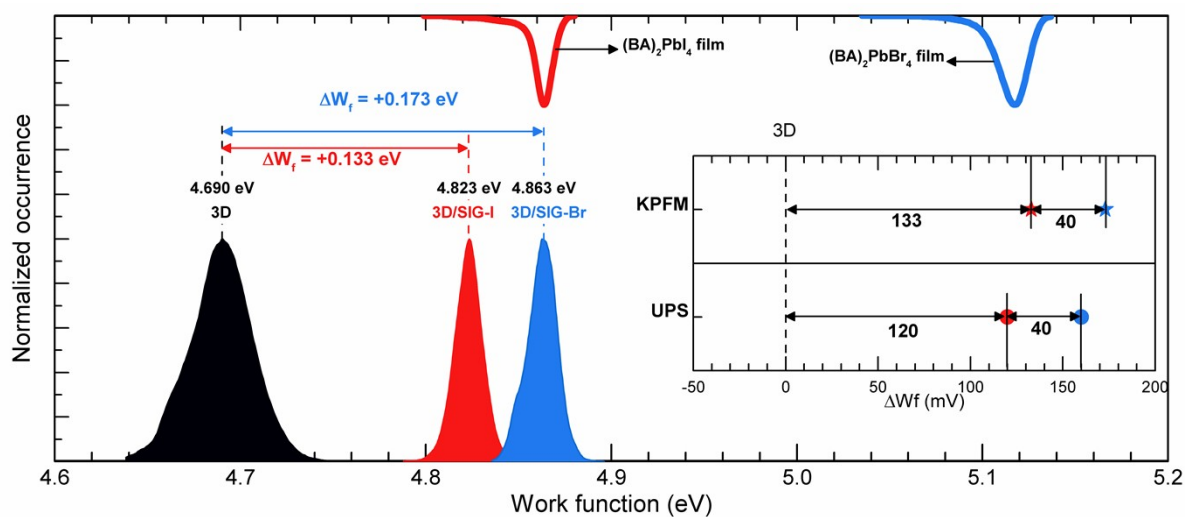
Figure S15. Energy level characterization of 3D/SIG-2D bilayer using KPFM measurement in dark. Work function distribution for 3D, 3D/SIG-I, and 3D/SIG-Br films on FTO/SnO$_2$. The upper distribution, marked in red and blue, indicates the pure 2D perovskite on ITO. The inset figure shows the differences in work function relative to the 3D perovskite.

Table S5. UPS results of energy level after 3D/SIG-2D junction for SIG-I and SIG-Br, respectively. The vacuum level shift (ΔE_{vac}) and aligned VBM values were estimated based on aligned work function.

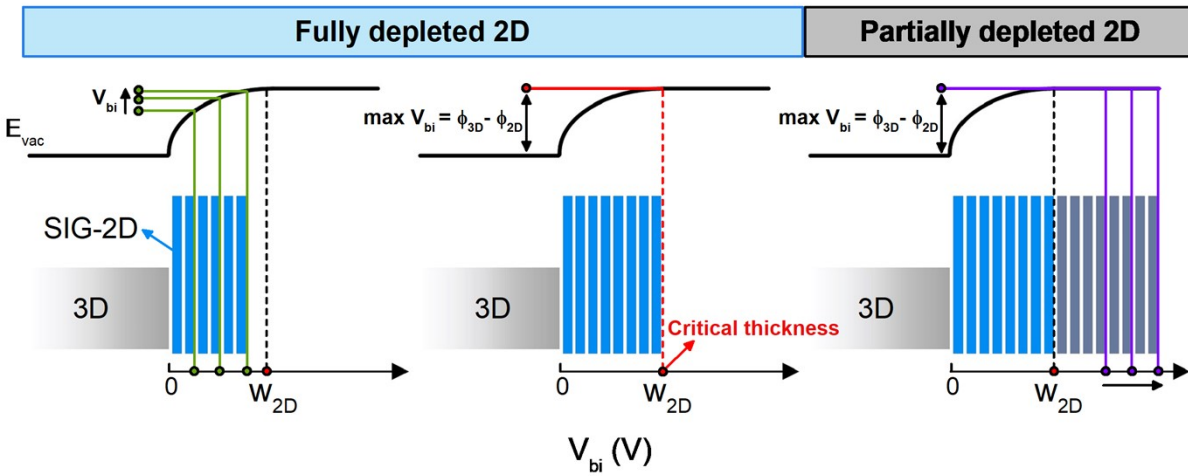|	ϕ (eV)	IE - ϕ (eV)	ΔE_{vac} (eV)	Aligned VBM (eV)
3D	-4.82	0.71	-	-5.53
3D/SIG-I	-4.94	0.61	+0.12	-5.43
3D/SIG-Br	-4.98	0.50	+0.16	-5.31

Figure S16. P-p isotype heterojunction of 3D/SIG-2D bilayer.
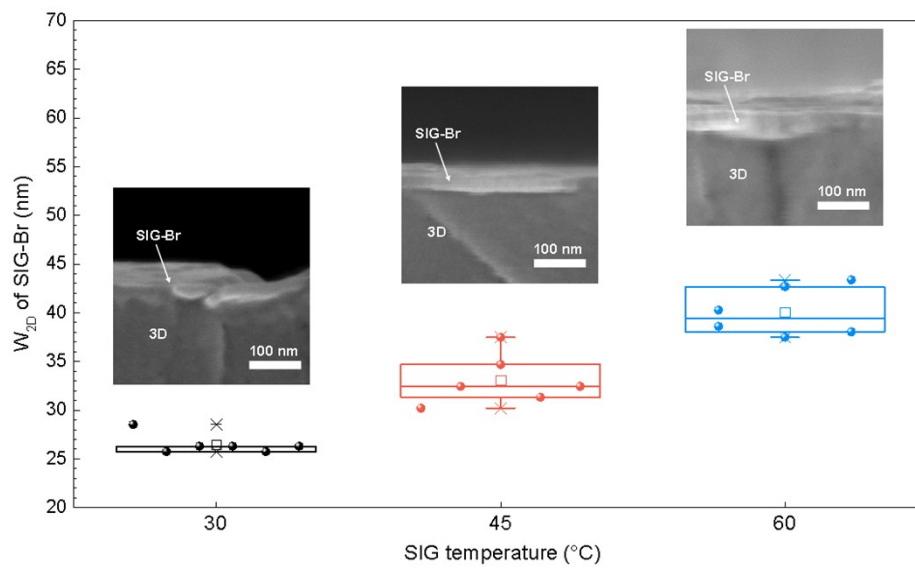
Figure S17. SIG-Br thickness as a function of the SIG process temperature. The thicknesses (W_{2D}) of all SIG-Br layer were observed using cross-sectional Scanning Electron Microscopy (SEM).

	Scan Direction	Jsc [mA/cm^2]	Voc [V]	F.F [%]	PCE [%]	Average PCE [%]
26.5 nm	Forward	26.02	1.121	81.24	23.71	**23.90**
	Reverse	26.00	1.133	81.83	24.11	
33.1 nm	Forward	25.97	1.152	81.64	24.43	**24.43**
	Reverse	25.99	1.150	81.73	24.44	
40.1 nm	Forward	26.11	1.181	82.78	25.53	**25.47**
	Reverse	26.05	1.181	82.67	25.42	
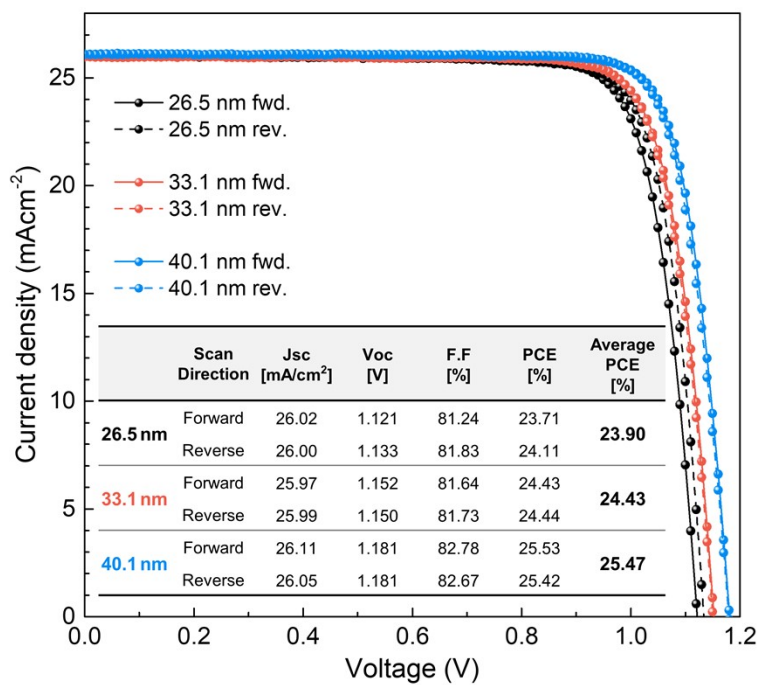
Figure S18. Device performance as a function of SIG-Br thickness. All photovoltaic devices were fabricated with the following structure: FTO/SnO$_2$/3D/SIG-Br/Spiro-OMeTAD/Au.
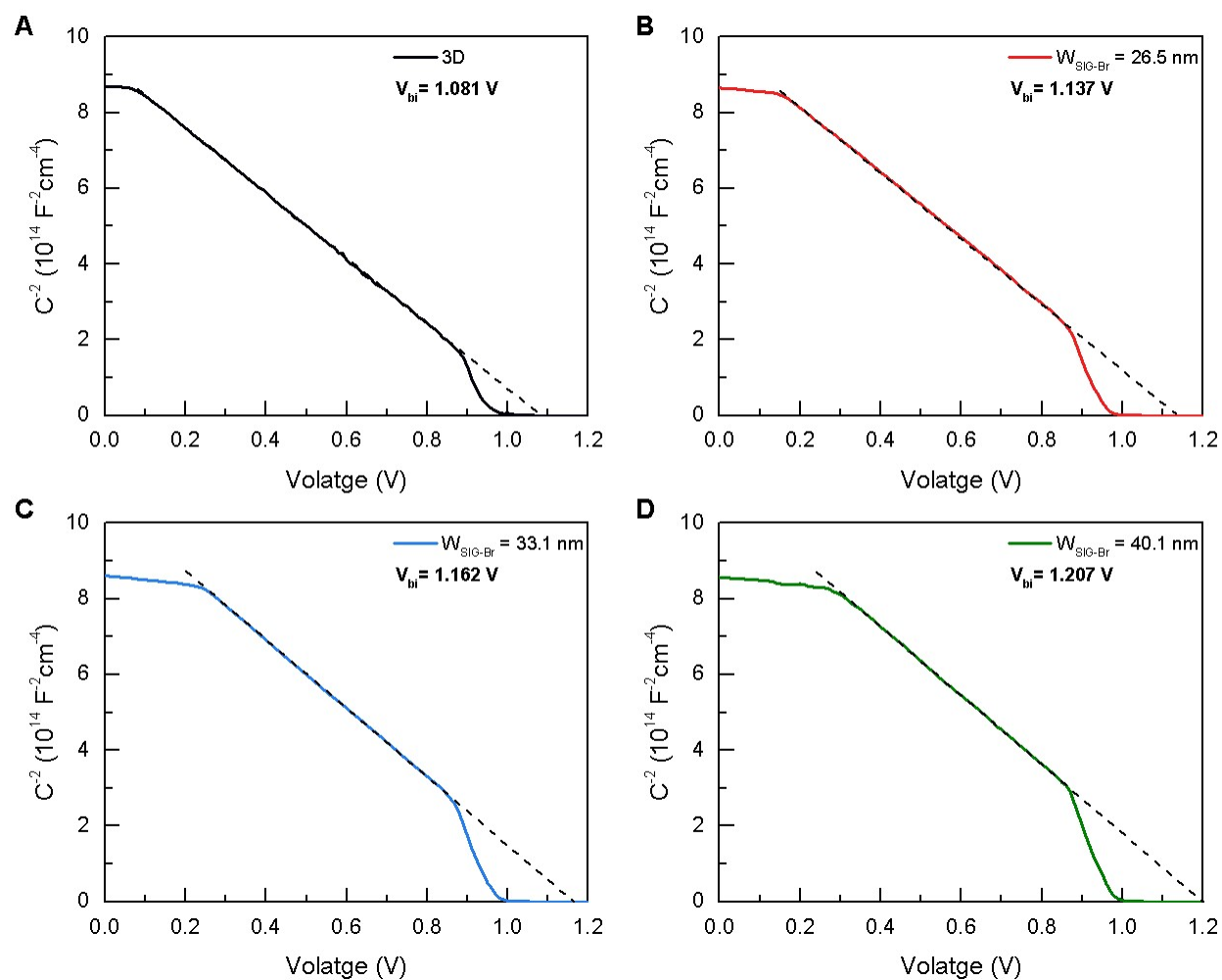
Figure S19. Mott-Schottky plot as a function of the SIG-Br thickness. The built-in potential (V_{bi}) was measured at 10 kHz in dark conditions for devices with (A) 3D, (B) W_{SIG-Br} = 26.5 nm, (C) W_{SIG-Br} = 33.1 nm, and (D) W_{SIG-Br} = 40.1 nm.
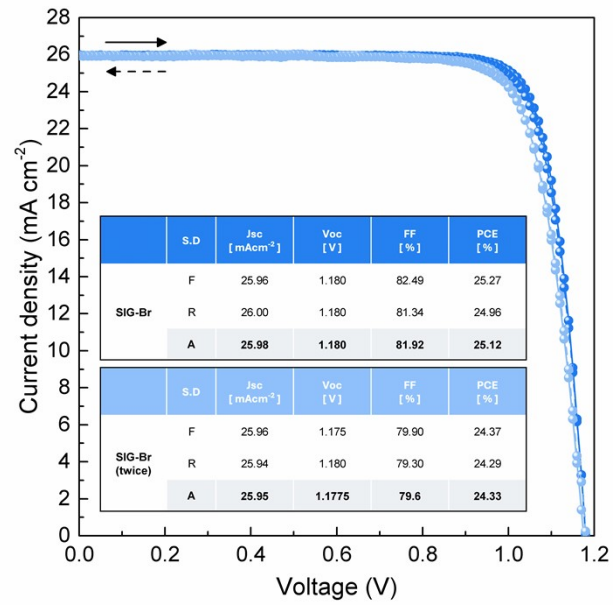
Figure S20. Current density – voltage curve according to the effect of multiple iterations of the SIG-Br process. All SIG processes were conducted at a temperature of 60 degrees Celsius.

	S.D	Jsc [mAcm^{-2}]	Voc [V]	FF [%]	PCE [%]
	F	25.96	1.180	82.49	25.27
SIG-Br	R	26.00	1.180	81.34	24.96
	A	25.98	1.180	81.92	25.12
	F	25.96	1.175	79.90	24.37
SIG-Br (twice)	R	25.94	1.180	79.30	24.29
	A	25.95	1.1775	79.6	24.33
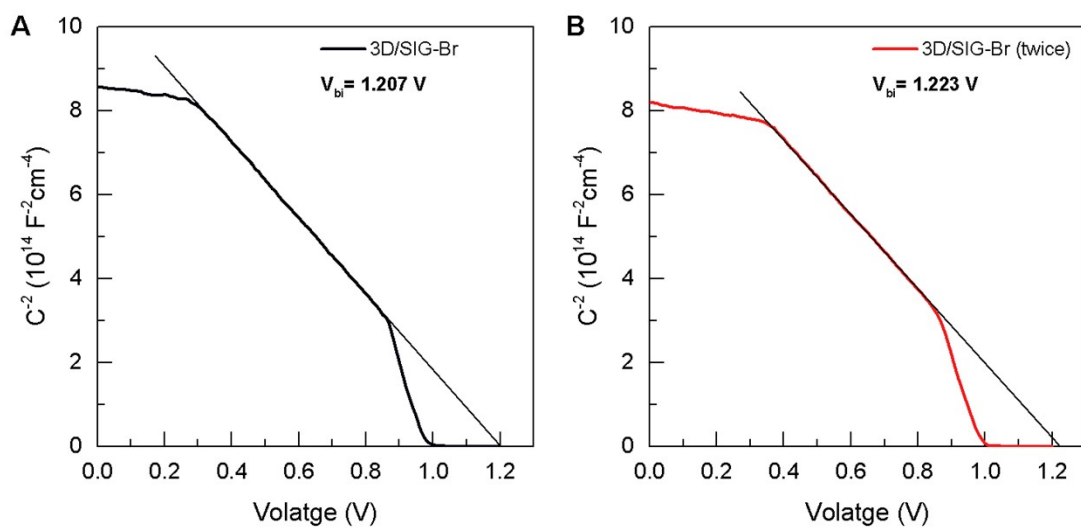
Figure S21. Mott-Schottky plot illustrating the effect of multiple iterations of the SIG-Br process. All SIG processes were conducted at a temperature of 60 degrees Celsius.

Note S1. P-p isotype heterojunction analysis

In the case of a p-p heterojunction, it can be analyzed using the continuity of electric displacement (D=εF), (where ε is the dielectric constant, and F is the electric field strength)[11]. The electric displacement in each semiconductor region can be calculated as follows, where x_0 represents the position of the interface and V_1 and V_2 mean the portion of applied voltage in first and second p-type semiconductor region, respectively:

For the first p-type semiconductor region with narrow gap, which is 3D perovskite in our junction.

$$D_{3D} = \epsilon_{3D}F_{3D}(x_0) = \left\{2\varepsilon_{3D}qN_{3D}\left[\frac{kT}{q}\exp\left(exp\frac{q}{kT}(V_{3D}-V_1)-1\right)-(V_{3D}-V_1)\right]\right\}^{1/2} \tag{1}$$

For the second p-type semiconductor region with wide gap, which is 2D perovskite in our junction.

$$D_{2D} = \epsilon_{2D}F_{2D}(x_0) = \left\{2\varepsilon_2qN_{2D}\left[(V_{D2}-V_2)\right]\right\}^{1/2} \tag{2}$$

At the interface, the continuity of the electric displacement requires that these two values matches, leading to the derivation of the following relationship equation when applied voltage was zero ($V_1 = V_2 = 0$):

$$2\varepsilon_{3D}qN_{3D}\left[\frac{kT}{q}\exp\left(exp\frac{q}{kT}(V_{3D})-1\right)-(V_{D1})\right] = 2\varepsilon_{2D}qN_{2D}\left[(V_{2D})\right] \tag{3}$$

In Equation (3), the total built-in potential (V_{bi}) across the p-p isotype heterojunction is the sum of the built-in potentials in each semiconductor ($V_{bi} = V_{3D} + V_{2D}$). If the concentrations of each semiconductor are defined, it becomes possible to track the changes in V_{3D} and V_{2D} as the concentration's variation. The V_t of the 3D/SIG-I and 3D/SIG-Br has been used the values for the vacuum level shift obtained from the UPS.

To calculate the ratio of V_{2D} based on the N_{2D}, we set the N_{3D} to 8.00×10^{10} cm^{-3} as reported in previous studies[12]. Relative dielectric constant of 3D, (BA)$_2$PbI$_4$, and (BA)$_2$PbBr$_4$ perovskite was set to be 30, 9.5, and 16.67 respectively[13, 14].

Note S2. Carrier concentrations of 2D perovskite

Consider the sheet concentrations (cm^{-2}) in valence band for p-type 2D semiconductor materials by using following equation[15, 16].

$$\sigma = \left(\frac{4\pi m_h}{h^2}\right)k_bTln\{1 + exp[-\frac{E_F - E_v}{k_bT}] \tag{4}$$

In equation (4), σ, m_h, and E_F-E_V are sheet concentration, effective hole mass and the energy level difference between Fermi level to valence band maximum, respectively. To estimate the sheet concentration, the m_h for (BA)$_2$PbI$_4$ and (BA)$_2$PbBr$_4$ of 0.111 and 0.090 were used according to the previous report[17]. The carrier concentration was then dimensionally corrected by the thickness of the monolayer of each 2D perovskite to derive the carrier concentration (cm^{-3})[15, 16].
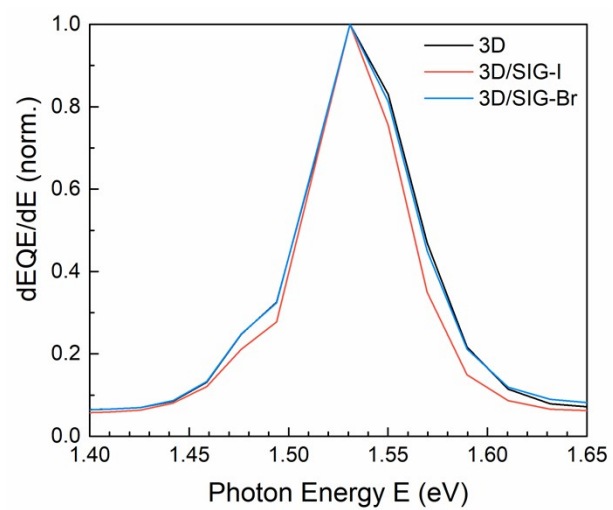
Figure S22. Photovoltaic band gap of all samples was calculated from EQE spectrum.
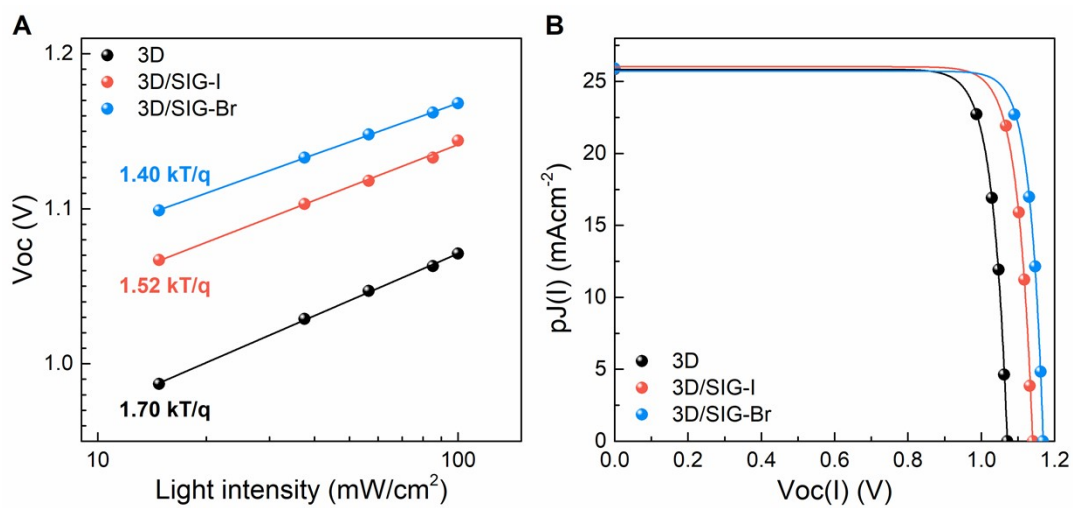
Figure S23. Open-circuit voltage as a function of light intensity and the pseudo-JV curve.

Measurement Report
Spectral Response Characteristics
Current-Voltage Characteristics

Report prepared for

School of Civil, Environmental and Architectural Engineering, Korea University

Report prepared by

National University of Singapore
Solar Energy Research Institute of Singapore

Block E3A, #06-01
7 Engineering Drive 1
Singapore 117574
SINGAPORE

Date: 18 August 2023
Reference: No Quote
Document ID: SERIS-2023-CHAR-00000131-271-03
Supplementary Files: The reported data are also sent in digital, tabulated format.

Operator, Solar Cell Testing
Ms YE Jia Yi

Head, Solar Cell Testing
Dr CHOI Kwan Bum

21 Aug 2023
(Signature and Date)

21 Aug 2023
(Signature and Date)

This measurement report shall not be reproduced other than in full except with the permission of the Solar Energy Research Institute of Singapore (SERIS).

SERIS-2022-CHAR-00000131-271-03   Page 1 of 10

4.2 One-Sun Current-Voltage (I-V) Characteristics Measurement

The I-V parameters of the test solar cell are shown below.

Table 4. Main I-V parameters for the test solar cell

Sample ID	Open-circuit voltage V_{oc} (V)	Short-circuit current I_{sc} (mA)	Fill factor FF (%)	Area A (cm^2)	Efficiency η (%)
C4 Averaged	1.174	2.53	82.76	0.097	25.37
Forward	1.173	2.54	82.41	-	25.26
Reverse	1.175	2.53	83.14	-	25.48

Table 5. Other I-V parameters for the test solar cell

Sample ID	Voltage at max. power V_{mpp} (V)	Current at max. power I_{mpp} (mA)	Maximum power P_{mpp} (mW)	Short-circuit current density J_{sc} (mA/cm^2)	Mismatch correction factor
C4 Averaged	1.016	2.42	2.46	26.11	1.0046
Forward	1.013	2.42	2.45	26.13	-
Reverse	1.018	2.43	2.47	26.10	-

The I-V parameters are computed from average of the forward and reverse I-V sweep measurements, performed at a sweep rate of 0.10 V/s. The relative difference of FF for forward and reverse I-V sweep at this sweep rate was about 1%.
The I-V parameters reported are applicable to the time of the test, and do not imply future performance.

The plot of the test solar cell I-V characteristics is shown below.
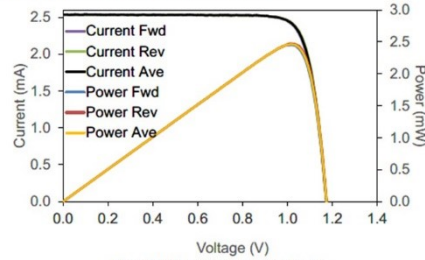
Figure 2. I-V characteristics of test solar cell

SERIS-2022-CHAR-00000131-271-03   Page 6 of 10

Figure S24. Independent certification from Solar Energy Research Institute of Singapore.
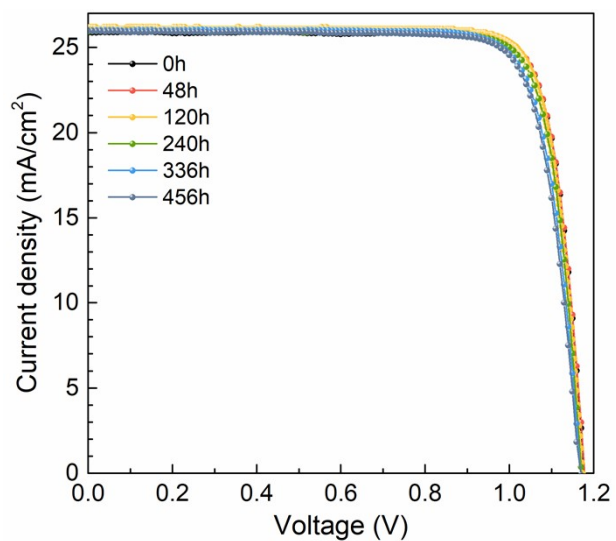
Figure S25. Storage stability performance of 3D/SIG-Br device.

Table S6. Storage stability PV parameters of 3D/SIG-Br device.

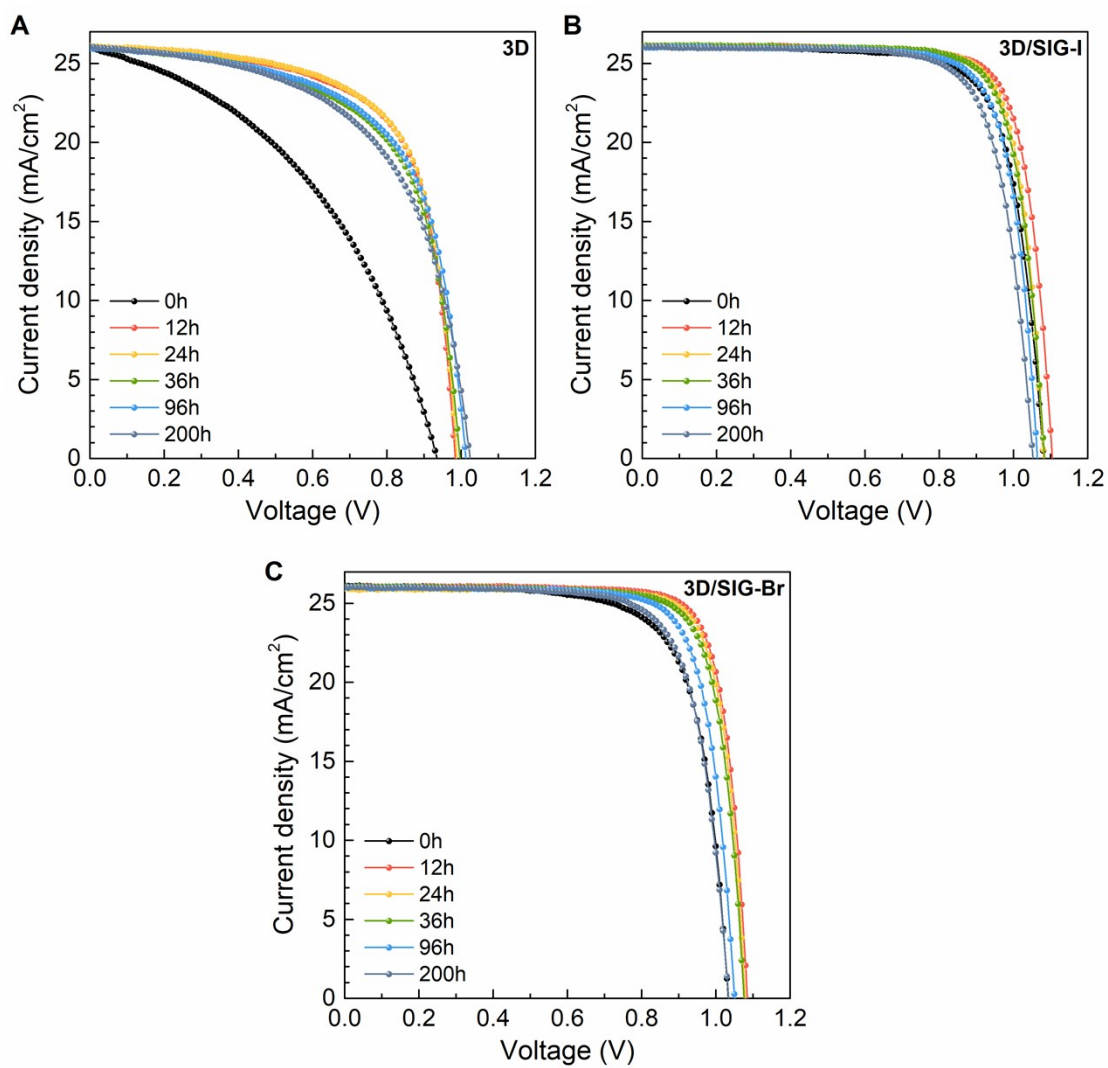| Time (h)	J_{SC} (mA/cm²)	V_{OC} (V)	FF (%)	PCE (%)
0	25.88	1.178	83.07	25.32
48	25.97	1.180	82.58	25.39
120	26.11	1.174	82.76	25.37
240	25.97	1.172	82.33	25.07
336	26.01	1.166	81.18	24.61
456	25.97	1.168	80.95	24.55

Figure S26. Average thermal stability performance for all devices at 85℃.

Table S7. Thermal stability PV parameters of the 3D, 3D/SIG-I and 3D/SIG-Br devices at 85℃

Time (h)	J_{SC} (mA/cm^2)	V_{OC} (V)	FF (%)	PCE (%)	Ratio of stabilized PCE
3D					
0	25.97	0.928	40.13	9.68	-
12	25.95	0.978	65.26	16.57	1.00
24	26.00	0.983	64.33	16.45	0.99
36	25.95	1.007	61.16	15.98	0.96
100	25.93	1.025	58.14	15.45	0.93
200	25.90	1.016	52.48	13.83	0.83
3D/SIG-I					
0	26.05	1.043	70.58	19.19	-
12	26.03	1.079	80.02	22.47	1.0
24	25.91	1.073	79.66	22.15	0.99
36	26.04	1.070	77.89	21.70	0.97
100	26.03	1.073	76.71	21.42	0.95
200	25.99	1.057	74.08	20.35	0.91
3D/SIG-Br					
0	26.06	1.067	75.60	21.06	-
12	26.08	1.101	78.39	22.51	1
24	26.03	1.081	79.12	22.27	0.99
36	26.07	1.078	78.28	22.00	0.98
100	25.99	1.074	77.38	21.61	0.96
200	26.02	1.053	75.55	20.69	0.92
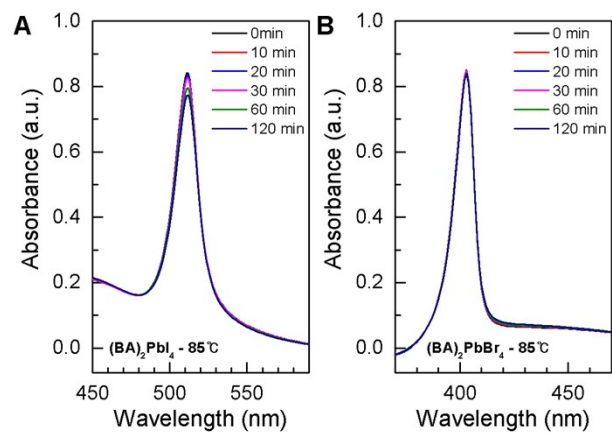
Figure S27. Thermal stability test of (BA)$_2$PbI$_4$ and (BA)$_2$PbBr$_4$ films on ITO glass. All sample are tested without any encapsulation.

A

Intensity (a.u.)

(4FPEA)$_2$PbI$_4$

W$_f$=5.05 eV

17.0　16.5　16.0　15.5　15.0
Binding energy (eV)

B

Intensity (a.u.)

(4FPEA)$_2$PbI$_4$

IE-W$_f$ = 1.05 eV

1.5　1.0　0.5　0.0
Binding energy (eV)

C

Current density (mA cm^{-2})

Voltage (V)

(4FPEA)$_2$PbI$_4$

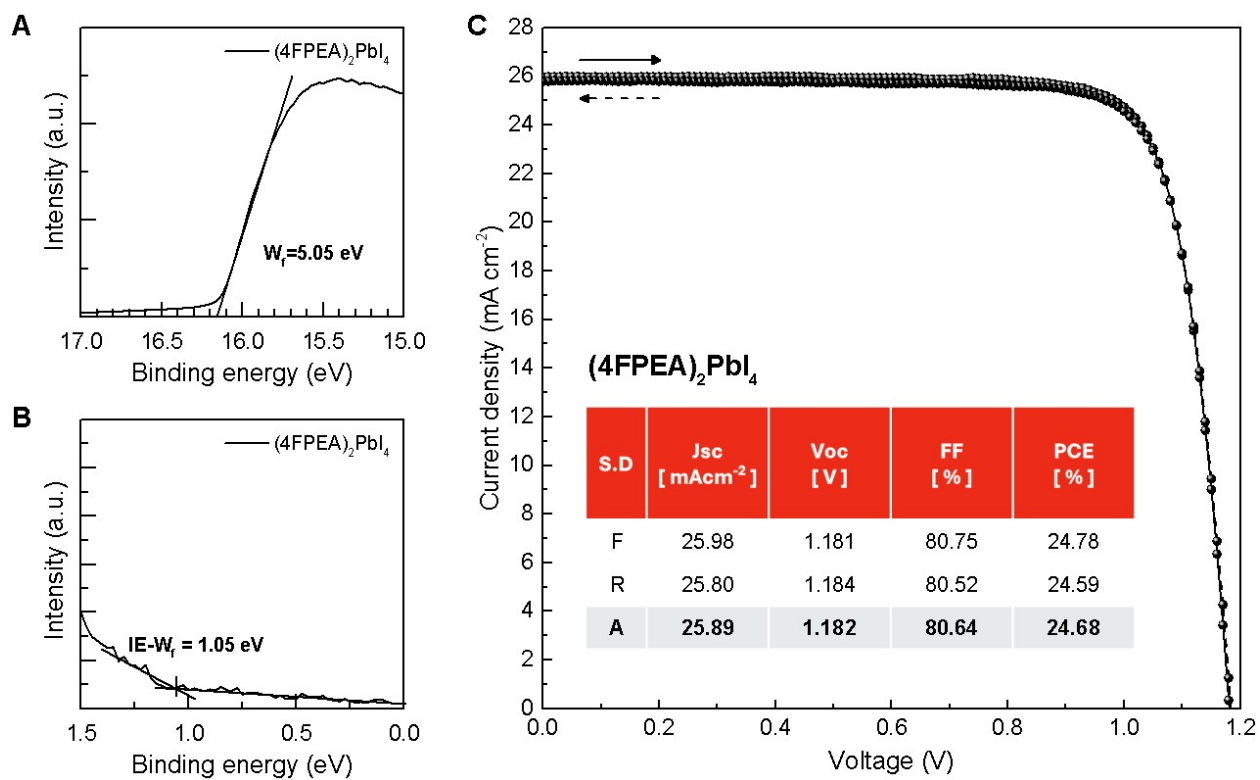| S.D	Jsc [mAcm^{-2}]	Voc [V]	FF [%]	PCE [%]
F	25.98	1.181	80.75	24.78
R	25.80	1.184	80.52	24.59
A	**25.89**	**1.182**	**80.64**	**24.68**

Figure S28. Characterization of (4FPEA)$_2$PbI$_4$ film and J-V curve for 3D/SIG-(4FPEA)$_2$PbI$_4$ device.

Supplemental references

1. K. P. Goetz, A. D. Taylor, F. Paulus and Y. Vaynzof, *Advanced Functional Materials*, 2020, **30**, 1910004.

2. S. Tan, T. Huang, I. Yavuz, R. Wang, T. W. Yoon, M. Xu, Q. Xing, K. Park, D.-K. Lee and C.-H. Chen, *Nature*, 2022, **605**, 268-273.

3. C. Cho, Y.-W. Jang, S. Lee, Y. Vaynzof, M. Choi, J. H. Noh and K. Leo, *Science advances*, 2021, **7**, eabj1363.

4. M. Fischer, K. Tvingstedt, A. Baumann and V. Dyakonov, *ACS Applied Energy Materials*, 2018, **1**, 5129-5134.

5. L. Shi, M. P. Bucknall, T. L. Young, M. Zhang, L. Hu, J. Bing, D. S. Lee, J. Kim, T. Wu, N. Takamure, D. R. McKenzie, S. Huang, M. A. Green and A. W. Y. Ho-Baillie, *Science*, 2020, **368**, eaba2412.

6. R. Lin, J. Xu, M. Wei, Y. Wang, Z. Qin, Z. Liu, J. Wu, K. Xiao, B. Chen, S. M. Park, G. Chen, H. R. Atapattu, K. R. Graham, J. Xu, J. Zhu, L. Li, C. Zhang, E. H. Sargent and H. Tan, *Nature*, 2022, **603**, 73-78.

7. T. Li, J. Xu, R. Lin, S. Teale, H. Li, Z. Liu, C. Duan, Q. Zhao, K. Xiao, P. Wu, B. Chen, S. Jiang, S. Xiong, H. Luo, S. Wan, L. Li, Q. Bao, Y. Tian, X. Gao, J. Xie, E. H. Sargent and H. Tan, *Nat Energy*, 2023, DOI: 10.1038/s41560-023-01250-7.

8. W. Zhang, S. Pathak, N. Sakai, T. Stergiopoulos, P. K. Nayak, N. K. Noel, A. A. Haghighirad, V. M. Burlakov, D. W. deQuilettes, A. Sadhanala, W. Li, L. Wang, D. S. Ginger, R. H. Friend and H. J. Snaith, *Nature Communications*, 2015, **6**, 10030.

9. J. Park, J. Kim, H.-S. Yun, M. J. Paik, E. Noh, H. J. Mun, M. G. Kim, T. J. Shin and S. I. Seok, *Nature*, 2023, **616**, 724-730.

10. G. Kim, H. Min, K. S. Lee, D. Y. Lee, S. M. Yoon and S. I. Seok, *Science*, 2020, **370**, 108-112.

11. R. L. Anderson, *Solid-State Electronics*, 1962, **5**, 341-351.

12. O. Gunawan, S. R. Pae, D. M. Bishop, Y. Virgus, J. H. Noh, N. J. Jeon, Y. S. Lee, X. Shao, T. Todorov and D. B. Mitzi, *Nature*, 2019, **575**, 151-155.

13. H. Tsai, W. Nie, J.-C. Blancon, C. C. Stoumpos, R. Asadpour, B. Harutyunyan, A. J. Neukirch, R. Verduzco, J. J. Crochet and S. Tretiak, *Nature*, 2016, **536**, 312-316.

14. X. Xu, Y. Wu, Y. Zhang, X. Li, F. Wang, X. Jiang, S. Wu and S. Wang, *Energy & Environmental Materials*, 2024, **7**, e12487.

15. J.-W. Chen, S.-T. Lo, S.-C. Ho, S.-S. Wong, T.-H.-Y. Vu, X.-Q. Zhang, Y.-D. Liu, Y.-Y. Chiou, Y.-X. Chen and J.-C. Yang, *Nature Communications*, 2018, **9**, 3143.

16. N. Ma and D. Jena, *2D Materials*, 2015, **2**, 015003.

17. S. Silver, J. Yin, H. Li, J. L. Brédas and A. Kahn, *Advanced Energy Materials*, 2018, **8**, 1703468.